

The genetic driver of Acute Necrotizing Encephalopathy, *RANBP2*, regulates the inflammatory response to Influenza A virus infection

Received: 5 May 2025

Accepted: 28 January 2026

Published online: 06 February 2026

 Check for updatesSophie Desgraupes¹, Adrien Decorsière¹, Suzon Perrin¹, Benoît Gouy¹, Yifan E. Wang², Alexander F. Palazzo², Sandie Munier³ & Nathalie J. Arhel¹✉

Influenza virus infections can cause severe complications such as Acute Necrotizing Encephalopathy (ANE), which is characterised by a rapid onset of pathological inflammation following febrile infection. Heterozygous dominant mutations in the nucleoporin *RANBP2*/*Nup358* predispose to influenza-triggered ANE1. The aim of our study was to determine whether *RANBP2* plays a role in IAV-triggered inflammatory responses. We found that the depletion of *RANBP2* in a human airway epithelial cell line increases IAV genomic replication by favouring the import of the viral polymerase subunits, PB1, PB2, and PA, following viral transcription and translation. Additionally, *RANBP2* knockdown enhances the cytoplasmic export of viral genomic RNA (vRNA) and disrupts segment stoichiometry, which is associated with elevated production of the pro-inflammatory chemokines CXCL8, CXCL10, CCL2, CCL3, and CCL4 in human primary macrophages. Using CRISPR-Cas9 knock-in for the ANE1 disease variant *RANBP2*-T585M, we further demonstrate that this point mutation causes a loss-of-localisation phenotype that excludes *RANBP2* from the nuclear envelope, which phenocopies *RANBP2* knockdown by increasing IAV replication and driving pro-inflammatory cytokine expression following infection. Together, our results reveal that *RANBP2* regulates influenza RNA replication and nuclear export, thereby restraining virus-induced hyperinflammation, and further suggest that ANE1 pathogenesis results from the impaired localisation of *RANBP2* at the nuclear envelope.

Influenza viral infections are responsible for seasonal epidemics with respiratory manifestations but can also lead to severe complications. Among these, Acute Necrotizing Encephalopathy (ANE), also called ANE of Childhood (ANEC), is a severe reaction to febrile infection that is characterized by rapid progression and very poor prognosis^{1–4}. Influenza viruses are thought to be responsible for ~50% of all ANE episodes and are associated with high morbidity and mortality^{4–9}.

Although the pathogenesis is unclear, a hyperinflammatory response triggered by the virus is proposed as the underlying mechanism^{4,10,11}, and early anti-inflammatory therapy may help mitigate the disease^{8,12,13}.

Influenza viruses belong to the *Orthomyxoviridae* family and are classified into types, with Influenza A and B being the most prevalent ones associated with seasonal flu cases. Influenza A is further divided into subtypes based on their surface glycoproteins, haemagglutinin

¹Institut de Recherche en Infectiologie, University of Montpellier, Montpellier, France. ²Department of Biochemistry, University of Toronto, Toronto, ON, Canada. ³Institut Pasteur, Université Paris Cité, Unité Lyssavirus, Épidémiologie et Neuropathologie, Paris, France. ✉e-mail: nathalie.arhel@cnrs.fr

(HA) and neuraminidase (NA). The H1N1 and H3N2 strains are responsible for major outbreaks and epidemics, and in the 2024-2025 winter season, there has been an unprecedented surge in H1N1 cases, leading to an unusual spike in hospitalizations and ANE in children⁵.

The Influenza A virus (IAV) is an enveloped particle containing 8 negative-sense single-stranded genomic viral RNA (vRNA) segments, each packaged by nucleoprotein (NP) into a viral ribonucleoprotein (vRNP) complex, and associated with the viral polymerase complex (PB1, PB2, and PA). Unlike most RNA viruses, IAV replicates in the nucleus and hijacks the nuclear pore complex (NPC) machinery for four critical steps of its replication cycle. (i) After endocytosis and uncoating, vRNPs are trafficked to the nucleus, where the viral polymerase transcribes the viral genome. (ii) Capped and polyadenylated mRNAs are exported into the cytoplasm for translation by cytoplasmic ribosomes. (iii) The newly translated viral proteins, including NP, PB1, PB2, and PA, are imported back into the nucleus, which allows the viral polymerase to replicate the viral genome into complementary RNAs (cRNA) and genomic vRNA. (iv) Lastly, new vRNPs, assembled with M1 and NS2/NEP, are exported back from the nucleus for incorporation into budding virions^{14–17}.

Many viral and host factors are thought to contribute to severe influenza, and genetic susceptibility, particularly in genes that regulate innate signalling and antiviral response, has been reported^{18–20}. However, the mechanisms that drive severe influenza-triggered ANE in previously healthy children are not known. One clue to understanding the pathogenesis of influenza-associated ANE comes from genetic susceptibility in familial, recurrent cases, known as ANE1 (or ADANE)⁷. Patients with ANE1 present with autosomal dominant missense mutations in *RANBP2* and have a significantly increased lifetime risk of developing ANE²¹. Mutations in *RANBP2* increase the risk of relapse and recurrence^{8,10} and may be associated with greater morbidity and mortality.

RANBP2 (Nup358) is a cytoplasmic fibril (CF) nucleoporin that regulates nucleocytoplasmic transport (NCT) by interacting with nuclear transport receptors such as Karyopherin α/β and CRM1/Exportin 1^{22,23}. Additional functions have been attributed to *RANBP2* at the NPC, many of which are linked to its C-terminal domain (CTD) E3 SUMO ligase activity, and away from the NPC, namely at annulate lamellae, mitochondria-endoplasmic reticulum junctions and in the nucleus²⁴. Moreover, at least 4 protein isoforms have been identified for *RANBP2*, however, it is not known if these have distinct functions or subcellular localisations²⁵. The predominant ANE1-associated mutation (c.C1754T on the coding DNA reference sequence, leading to p.T585M at the protein level), and most other pathogenic mutations in *RANBP2*, all cluster in the N-terminal domain (NTD), which is responsible for anchoring to NPCs^{6,26}. This suggests that the localization of *RANBP2* to CF of NPC may be physiologically essential, although no changes in localisation could be demonstrated following the overexpression of disease variants^{27,28}.

Previous work showed that *RANBP2* can modulate viral infection of several viruses, such as Adenovirus²⁹, Herpes simplex virus type 1 (HSV-1)^{30,31} and Human immunodeficiency virus type 1 (HIV-1)^{32–35}, however no work has uncovered a role for *RANBP2* in Influenza virus infection. In fact, although some studies showed that NPC components can impact the replication and transcription of Influenza virus, such as Nup62, Nup98, and Nup153, *RANBP2* was not identified as a host factor for Influenza virus^{36–38}.

Previous work also showed that *RANBP2* can modulate innate immune signalling, however this activity was consistently attributed to its E3 SUMO ligase activity or Cyclophilin-homology motif in the CTD^{27,39–41}, and no work has yet demonstrated a role for the NTD where ANE1 mutations are clustered.

The aim of our study was to determine how *RANBP2* contributes to or regulates inflammatory responses to infection by Influenza virus.

We show that *RANBP2* impacts the replication of genomic vRNA of IAV into cRNA by controlling the re-import of newly translated viral polymerase complex. In addition, *RANBP2* knockdown enhances cytoplasmic vRNA export and disrupts segment stoichiometry, thereby enhancing IAV-triggered inflammation. Notably, the predominant ANE1-associated variant T585M causes relocation of *RANBP2* away from the nuclear envelope, which phenocopies knockdown of *RANBP2* by increasing vRNA replication and export, and triggering hyperinflammation, which could provide a first clue in understanding the pathogenesis of ANE.

Results

Knockdown of *RANBP2* stimulates non-productive Influenza vRNA replication in infected cells

To investigate the role of *RANBP2* in IAV infection, *RANBP2* knockdown (*RANBP2*-KD) was induced in A549 human alveolar cells by lentiviral vector (LV) transduction of short hairpin RNAs (shRNAs) before infection with A/WSN/1933 (H1N1) virus at MOI 0.5. Supernatants were harvested at 10 h post-infection (hpi) to investigate the production of infectious viral particles by TCID50 titration. No differences were observed between the control and *RANBP2*-KD cells, suggesting that *RANBP2* had no effect on the production of infectious particles (Figs. 1a, S1a, b).

However, an unexpected phenotype was observed for the quantification of influenza virus RNAs in both A549 and the monocytic cell line THP-1. Infection kinetics were performed, and viral RNA levels were determined at early (2 h) and late (6, 8, 16, and 24 h) time points using qPCR primers recognizing M1 on segment 7. In A549 cells (Fig. 1b) and in the monocytic cell line THP-1 (Figs. 1c, S1c), a significant increase in M1 RNA was induced in *RANBP2*-KD cells. The increase in viral RNAs was confirmed in A549 cells with another IAV segment, encoding the NP (Fig. 1d), and appeared to be specific since no increase was observed for any of the housekeeping genes that were measured (Fig. 1e). Together, these data suggested that *RANBP2* is involved in controlling the synthesis of influenza RNAs but that this does not translate into increased productive infection.

Because different types of viral RNAs are produced during the IAV life cycle, we investigated which ones are impacted by the depletion of *RANBP2*. Sequence-tagged RT primers were used to specifically recognize the negative-sense genomic vRNA sequence or the positive-sense cRNA sequence for reverse transcription (RT) (Fig. S2a). First, the specificity of each primer was validated by amplifying only vRNA after vRNA-specific RT, or only cRNA after cRNA-specific RT, while not amplifying any target in non-infected cells (Fig. S2b). In *RANBP2*-KD cells, we observed a significant increase of both vRNA and cRNA (Fig. 1f), thus showing that *RANBP2* is involved in IAV RNA replication. Although this was unexpected given the absence of phenotype in terms of viral production, the marked increase in vRNA and cRNA levels suggested an enhancement in viral genome replication.

Having observed an increase in genomic vRNA, we tested if this correlated with more newly produced vRNPs. As previously, A549 cells were transduced with control- or *RANBP2*-shRNAs then infected with IAV (MOI 0.5). At 8 hpi, the distribution of NP was investigated by immunofluorescence. Although export is ongoing in every condition, *RANBP2*-KD cells showed a striking increase in cytoplasmic NP compared to control (Figs. 1g, h, S3). This phenotype was confirmed using a previously published *RANBP2*-targeting shRNA (Di Nunzio et al., 2012) and only in cells expressing the shRNA (Fig. S4a–d). In order to determine if signal corresponded to vRNPs or free NP in the cytoplasm, we performed co-stainings with other components of vRNPs (i.e. PB1 and PA). We observed a co-localisation of cytoplasmic NP with PB1 and with PA, with a Pearson coefficient >0.8 (Figs. 1i–k, S5a–d), indicating that *RANBP2*-KD induces an increase in vRNPs exported to the cytoplasm.

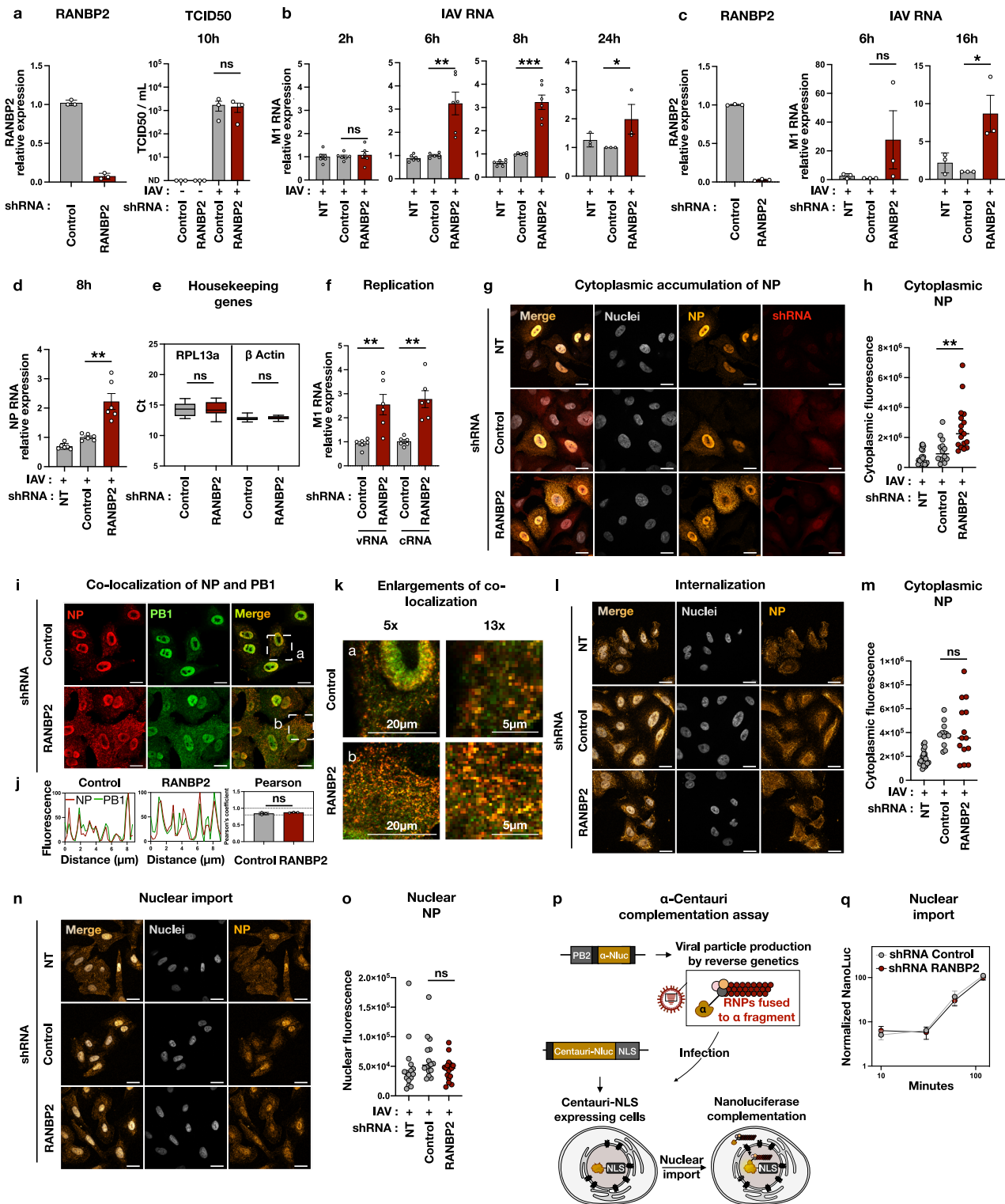


Fig. 1 | RANBP2 knockdown stimulates non-productive Influenza vRNA replication without affecting the initial vRNP nuclear import. **a** RANBP2 transcript levels (normalized to RPL13a and control) in A549 cells, and viral titre in MDCK cells, after transduction with control or RANBP2 shRNA, and infection with IAV (A/WSN/1933; MOI 0.5). Viral RNA levels for M1 or NP segments in A549 (**b**, **d**) or THP-1 (**c**) cells at the indicated time points: **b**: 6 h, $p = 0.0023$; 8 h, $p = 0.0008$; 24 h, $p = 0.0444$; **c**: $p = 0.015$; **d**: $p = 0.0046$. RANBP2 knockdown was confirmed by RT-qPCR in THP-1 cells (**c**), normalized as in (**a**). **e** Expression of housekeeping genes (RPL13a, $n = 18$; β -Actin $n = 12$). **f** Strand-specific quantification of vRNA ($p = 0.0063$) and cRNA ($p = 0.0014$) at 6 hpi. NP and PB1 localization in infected A549 cells at

8 hpi (MOI 0.5; **g**, **k**), 1 hpi (MOI 4; **l**, **m**) or 2 hpi (MOI 4; **n**, **o**) ($n = 3$; 12–17 cells per condition). For quantifications, each dot represents a single cell fluorescence normalized by area (**h**: $p = 0.0024$). Additional fields are shown in Fig. S3. **p**, **q** α -Centauri assay schematic and luminescence readout for nuclear import of vRNP (MOI 4). NanoLuc complementation results normalized to last time point ($n = 4$). Data are shown as mean \pm SEM or box-and-whisker plots (median, 25th–75th percentiles, min/max). $n = 3$ for all panels, except (**b**) (time points 2, 6, 8 h) and (**d**, **f**) ($n = 6$). Scale bars: 20 μ m. Statistical tests: two-tailed Student's t tests (unpaired for **a**, **b**, **e**, **f**, **h**, **j**, **m**, **o**; paired for **c**, **d**). ns: non-significant.

Increased IAV replication does not result from enhanced viral entry into cells or into the nucleus

To determine how vRNA is increased in RANBP2-depleted cells, we first tested whether RANBP2 regulates IAV infection by modulating viral entry into cells and/or nuclei, thereby increasing the quantity of IAV RNA to be copied.

To assess whether RANBP2 regulates cell or nuclear entry, control or RANBP2-KD cells were infected with IAV (A/WSN/33) at high MOI of 4, in order to increase signal detection during early steps of the viral cycle, and NP localization was studied by immunofluorescence at 1 hpi to assess internalization, and at 2 h to monitor NP nuclear entry. Results indicate that depletion of RANBP2 from A549 cells affects neither internalization (Fig. 1l, m) nor nuclear import (Fig. 1n, o).

To further validate these findings, we adapted an Alpha-Centauri protein-complementation assay previously developed to monitor the nuclear import of HIV-1⁴². Briefly, the NanoLuc protein was expressed as two unequal non-luminescent fragments. The smaller fragment was fused to PB2 in IAV particles (IAV- α), while the larger fragment (Centauri) was fused to a NLS and expressed in A549 cells by LV transduction (Cen-NLS) (Figs. 1p, S6a, b). Upon vRNP nuclear import, the two fragments reconstitute a functional NanoLuc, generating a measurable signal upon addition of substrate (Fig. S6c). No significant differences in luminescence were detected between control and RANBP2-KD cells at 1 and 2 hpi, confirming that RANBP2 is not essential for vRNP nuclear import (Figs. 1q, S6d), thus demonstrating that RANBP2 does not regulate IAV vRNP nuclear import.

RANBP2 knockdown facilitates the nuclear import of the neo-synthesised viral polymerase complex proteins PB1, PB2 and PA

Since RANBP2 does not impact the quantity of template available for replication, we investigated whether it modulates the quantity or localisation of the polymerase complex subunits. First, the total levels of PB1, PB2, PA and NP were assessed by western blot at 8 hpi, however, no differences were observed between RANBP2-KD cells and control cells (Fig. 2a, b), suggesting that RANBP2 does not impact the translation of the viral polymerase complex.

Being an NPC component, we hypothesised that RANBP2 may control the replication of vRNA by regulating the import of the viral polymerase after translation. Therefore, we tested the impact of RANBP2 on the nuclear import of newly synthesised PB1, PB2, and PA subunits. To focus specifically on import, we inhibited vRNP export using a pharmacological inhibitor of CRM1, KPT-330/Selinexor. First, we confirmed that KPT-330 inhibits vRNP export (Fig. S7a), with negligible toxicity (Fig. S7b) and that inhibition operates from 5 hpi onwards (Fig. S7c). Then we performed subcellular fractionation followed by western blotting at 6 hpi to determine the localisation of the different polymerase subunits. Results revealed an increase in PB1, PB2 and PA protein levels in the nucleus (Fig. 2c, d), confirmed by the immunofluorescence detection of nuclear PB1 (Fig. 2e, f), indicating that the import of the neo-synthesised polymerase is facilitated in the absence of RANBP2.

RANBP2 depletion favours the export of vRNA segments to the cytoplasm and disrupts the segment stoichiometry

Having determined that RANBP2 controls IAV replication in the nucleus by regulating the import of the newly synthesised viral polymerase, we asked why the increase in vRNA and vRNP does not translate into an increased production of infectious particles (Fig. 1a). To address this, we performed strand-specific RT to distinguish vRNA and cRNA, as previously (Fig. S2a), then quantified the 8 IAV segments by qPCR to investigate segment stoichiometry (Fig. 2g, S8a, b). After sub-cellular fractionation, analysis of influenza virus RNA localization revealed that, while RANBP2 knockdown led to an overall increase of all cRNA segments in the nucleus (Fig. S9), it also led to an overall increase in the nuclear export of vRNA segments (Fig. 2h, i). This effect

disproportionally affected individual segments across experiments, as reflected by a higher standard deviation (Fig. 2j). These findings indicate that, while the depletion of RANBP2 increases the replication of all vRNA segments, it also promotes their uneven export to the cytoplasm, thereby disrupting segment stoichiometry.

Taken together, our results indicated that the knockdown of RANBP2 perturbs infection by IAV, first by facilitating the re-import of polymerase into the nucleus, which increases cRNA and vRNA, second by disproportionately favouring the export of vRNA segments into the cytoplasm. The dysregulation of both these steps may cause an abnormal accumulation of some vRNA segments in the cytoplasm, thus constituting potential pathogen-associated molecular patterns (PAMPs) that may be sensed by the infected cell.

RANBP2 knockdown exacerbates the inflammatory response to IAV infection in primary human macrophages

To investigate whether the abnormal cytoplasmic accumulation of vRNA, observed in RANBP2-depleted cells, might associate with increased inflammation, we measured the expression of inflammatory transcripts by qPCR. In both A549 and U2OS cells, RANBP2 depletion led to an upregulation of inflammatory transcripts, which was significant in both cell types for IL-6 and IL-1 β (Fig. 3a, b, S10a, b). These changes mirrored the increase in vRNA (Fig. S10c) and were confirmed using an independent RANBP2-targeting shRNA (Fig. S11). Interestingly, a modest increase in some of these transcripts was also observed in uninfected cells (Fig. 3a, b), likely reflecting low level activation triggered by lentiviral vector transduction, but this was not significant.

To confirm this at the protein level, primary monocytes were isolated from the PBMCs of healthy donors and differentiated into granulocyte-macrophage colony-stimulating factor (GM-CSF)-derived macrophages. After 7 days of differentiation, primary monocyte-derived macrophages (MDM) were CD3⁻ CD14⁺ CD16⁺ CD11b⁺ HLA-DR⁺ CD80⁻ (Fig. S12). We first determined that IAV can infect MDMs (Fig. S13a), and stimulate an effective immune response without additional pre-stimulation, triggering the synthesis of pro-inflammatory cytokines such as IL-6 and IL-1 β (Fig. S13b). MDM were then transduced with LVs coding for control or RANBP2 shRNA, and infected with IAV (Fig. S14a, b). Supernatants were collected at 24 hpi and the secretion of pro-inflammatory mediators was analysed by Multiplex Luminex assay using the manufacturer's pre-defined inflammatory panel. Strikingly, the knockdown of RANBP2 in the primary macrophages from two donors led to an exacerbated inflammatory response to IAV infection, with a stronger induction of the pro-inflammatory chemokines CXCL8, CXCL10, CCL2, CCL3 and CCL4 (Fig. 3c).

Together, these findings suggest that RANBP2 plays a critical role in modulating the inflammatory response to IAV infection by regulating vRNA replication, nucleocytoplasmic trafficking of viral polymerase subunits, and selective vRNA export. Results suggest that the abnormal accumulation of viral components in the cytoplasm amplifies inflammatory signalling, highlighting a potential mechanism underlying the pathogenesis of ANE.

The RANBP2-T585M ANE1 variant drives IAV replication and hyperinflammation following infection

Having identified a role of RANBP2 in controlling the IAV-triggered inflammation, we investigated if this function is compromised by the predominant ANE-associated mutation, c.C1754T, p.T585M. Heterozygous mutations in *RANBP2* are associated with increased susceptibility to ANE, however, it is not known how these affect protein function. Indeed, previous work showed that ANE1 mutations do not alter the structure of RANBP2²⁸, and that exogenously-expressed RANBP2-T585M still localises to the nuclear envelope^{27,28}.

We introduced the predominant mutation (c.C1754T, p.T585M) by CRISPR-Cas9 knock-in of U2OS cells (Fig. 4a). A total of 47 clones were

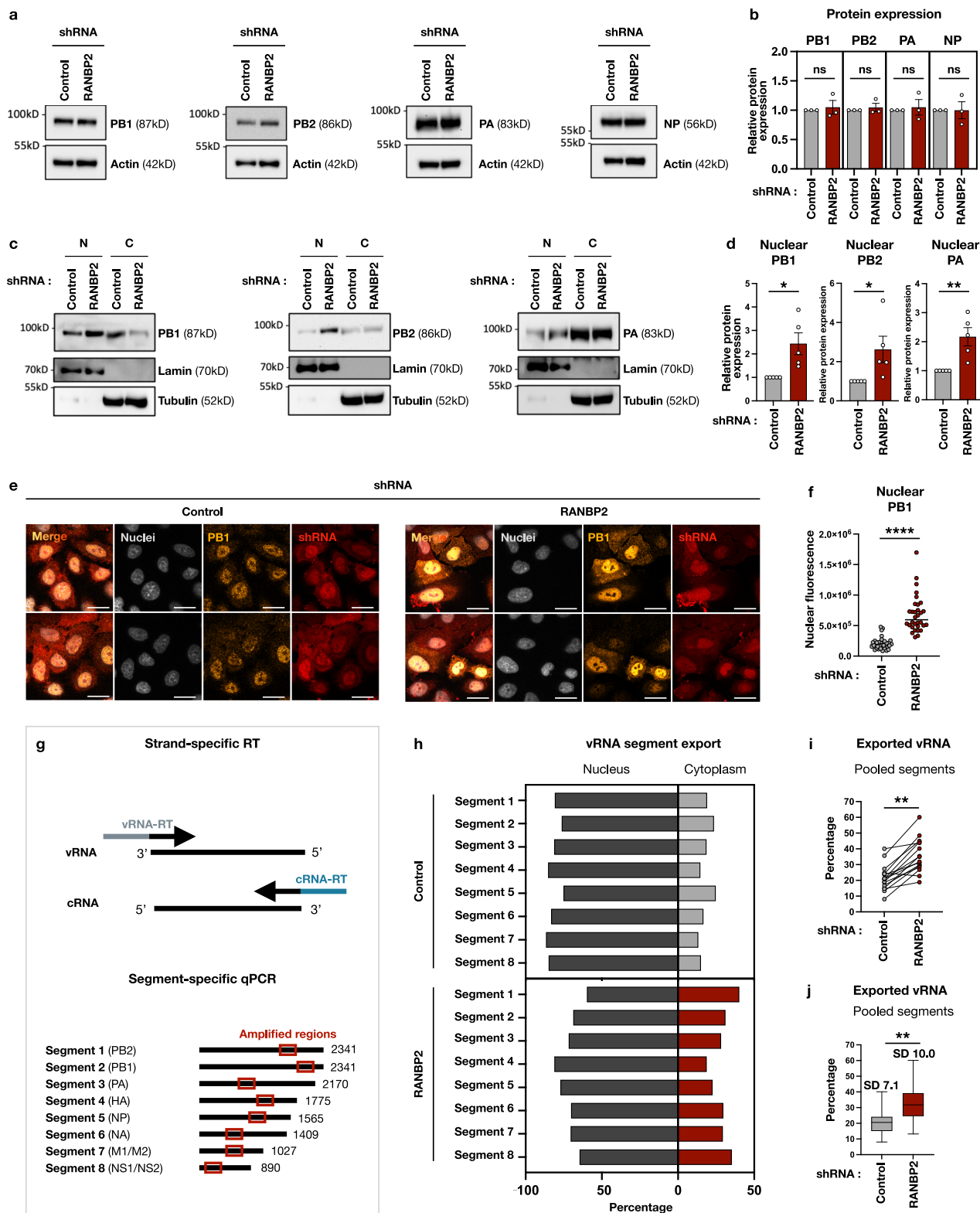


Fig. 2 | Enhanced reimport of viral polymerase complex proteins and cytoplasmic vRNP accumulation with disrupted segment stoichiometry upon RANBP2 knockdown. **a** PB1, PB2, PA and NP protein levels in A549 cells transfected with control or RANBP2 shRNA and infected with IAV (MOI 4) at 6 hpi. **b** Band intensities normalized to actin and control (mean \pm SEM; $n = 3$). **c** PB1, PB2 and PA levels in nuclear (N) and cytoplasmic (C) fractions after 2 h KPT-330 treatment and 6 h infection (MOI 0.5); lamin and tubulin used as fractionation controls. **d** Nuclear band intensities ($n = 5$) normalized to lamin and control (mean \pm SEM; PB1, $p = 0.0149$; PB2, $p = 0.0423$; PA, $p = 0.0059$). **e** PB1 staining in infected A549 cells at

6 hpi. Scale bar: 20 μ m. **f** Nuclear PB1 fluorescence quantification ($n = 3$; 32–34 cells per condition; $p < 0.0001$). **g** Strand- and segment-specific RTqPCR strategy for vRNA and cRNA amplification. Cytoplasmic and nuclear vRNA abundances for each segment at 6 hpi, expressed as percentages of their sum: representative experiment (**h**), all segments pooled (**i**) ($n = 2$, $p = 0.001$), or box-and-whisker plots (median, 25th–75th percentiles, min/max, and standard deviation (SD); $p = 0.001$). Dots represent biological replicates (mean of technical triplicates). Statistical tests: two-tailed unpaired Student's t -test (**b**, **d**, **f**) or Kolmogorov-Smirnov test (**i**, **j**). ns: non-significant.

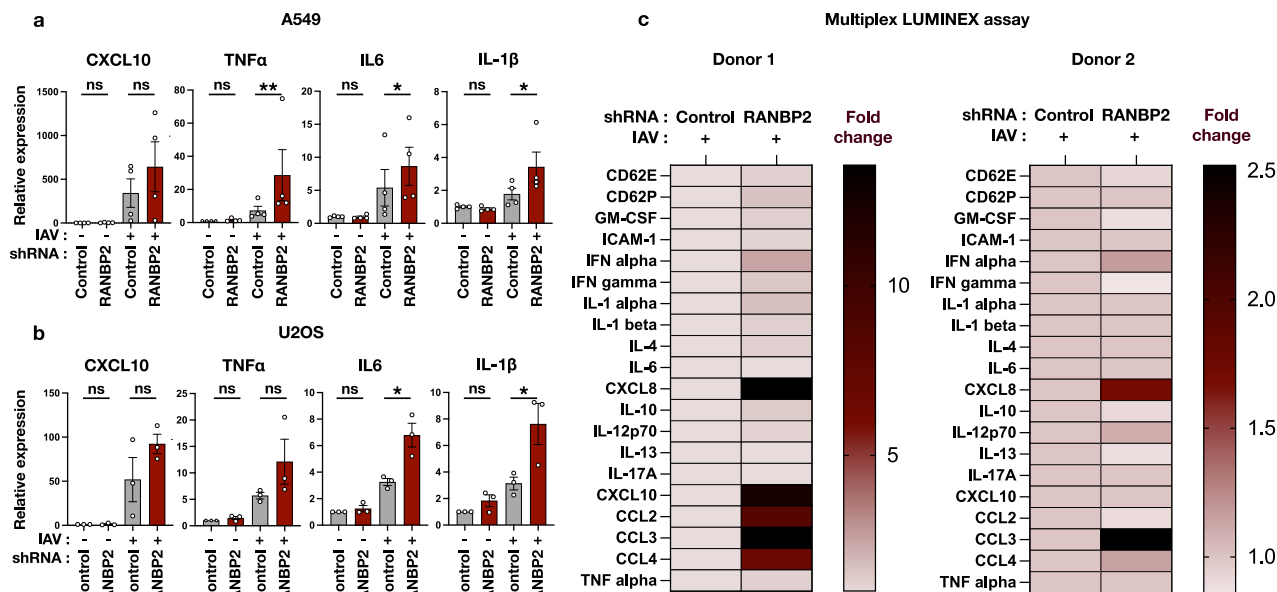


Fig. 3 | Inflammatory response to IAV infection upon RANBP2 knockdown. Cytokine transcript levels (normalized to RPL13a and uninfected control) in A549 (**a**) and U2OS (**b**) cells transfected with control or RANBP2 shRNA (MOI 30), and infected with IAV (MOI 0.5) overnight. Significant changes: TNF α ($p = 0.0045$), IL6 ($p = 0.0418$), IL1 β ($p = 0.019$) in A549 cells; IL6 ($p = 0.0158$), IL1 β ($p = 0.013$) in U2OS cells. **c** Inflammatory proteins in supernatants from IAV-stimulated monocyte-derived macrophages (MDM) from two donors at 24 h post-stimulation, quantified

by multiplex Luminex assay (samples diluted 1:50). Results shown as heat maps of mean fluorescence intensities (MFI) fold-change values relative to control. For qPCR quantifications (**a**, **b**), dots represent independent biological replicates ($n = 4$ for **a**; $n = 3$ for **b**), each corresponding to the mean of technical triplicates normalized to a housekeeping gene ($\Delta\Delta Ct$) and shown as mean \pm SEM. Statistical analyses were performed on biological replicates using two-tailed paired Student's *t* tests. ns: non-significant.

isolated after puromycin selection during 3 weeks. Mutations were confirmed by allelic qPCR (Figs. 4b, S15a–c), using a previously published protocol⁴³, and by Sanger sequencing of the cDNA (Fig. 4c, d). For many clones, we noted that CRISPR repair had occurred using the highly homologous RGPD sequences present on the same chromosome²⁴, rather than the repair plasmid, therefore only clones that did not recombine with RGPD were selected (Fig. S15b). In total, two wild-type clones (C4 and C15, referred to as WT/WT), one heterozygously-mutated (C10, WT/C1754T) and three homozygously-mutated (C6, C9 and C14, C1754T/ C1754T) clones were isolated.

CRISPR-knock-in clones were infected with IAV, and replication was assessed by quantifying viral NP at 8 hpi, as previously (Fig. 1g, h). Strikingly, cytoplasmic NP was significantly increased in all ANE1 CRISPR clones compared with wild-type clones, regardless of whether the mutation was heterozygous or homozygous (Figs. 4e, f, S16). qPCR analysis confirmed that both heterozygous and homozygous ANE1 genotypes exhibited a greater increase in IAV replication over time, with significantly higher vRNA levels at 24 hpi compared to WT clones (Figs. 4g, S17). Moreover, IAV infection induced an overall upregulation of inflammatory cytokines and chemokines, including CXCL10, IL-6, IL-1 β , CXCL8, and CCL3, with significantly higher overall expression in both heterozygous and homozygous ANE1 genotypes compared to WT clones (Figs. 4h, S18). Together, these results indicate that the ANE1-associated T585M mutation phenocopies RANBP2 knockdown by enhancing IAV replication and associated hyperinflammation.

In CRISPR-Cas9 T585M knock-in cells, RANBP2 mislocalises away from nuclear pores

Although previous studies reported that exogenously-expressed RANBP2-T585M localizes to the NPC^{27,28}, its expression and localization have not been examined in genetically edited cell lines. Overall, we did not observe a statistically significant variation in the protein levels of RANBP2 (Fig. S19a, b). We next examined the subcellular localisation of RANBP2 by immunofluorescence in the clones expressing RANBP2-

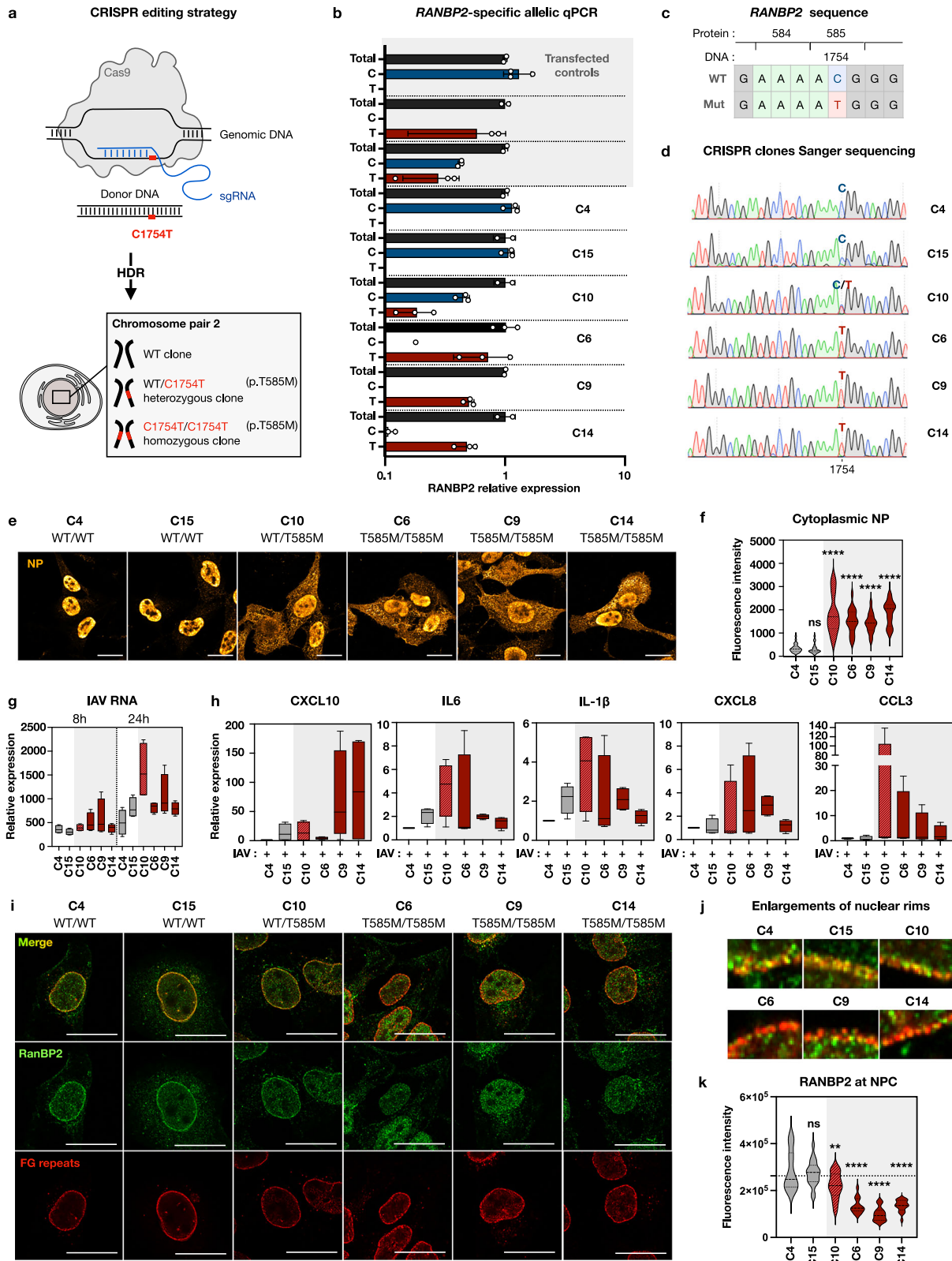
T585M heterozygously and homozygously using a RANBP2-specific antibody recognising the CTD. As expected, RANBP2 localised to the nuclear envelope in WT clones. In contrast, all three clones homozygous for RANBP2-T585M lost the characteristic nuclear rim staining, indicating that the mutation disrupts RANBP2 retention at the nuclear envelope (Fig. 4i, 4j). Despite this, nuclear pores appeared intact, since the labelling of FG-repeat Nups with the MAb414 antibody was comparable across all clones (Fig. 4i). In heterozygous clones, RANBP2 did localise at the nuclear envelope, although quantification revealed a modest but significant decrease compared to control clones, suggesting an intermediary phenotype (Fig. 4k).

In conclusion, our findings suggest that RANBP2 localization at the nuclear envelope is critical to safeguard cells from the pathological inflammation following viral infection. In ANE1, mutations in the NTD of RANBP2 are specifically associated with hyperinflammation.

Discussion

In this work, we show that the NPC component RANBP2 regulates the nucleocytoplasmic transport of IAV proteins and RNAs. Its absence from nuclear pores leads to exacerbated viral replication in the nucleus and dysregulated export of vRNA to the cytoplasm, resulting in the abnormal accumulation of vRNA segments that fail to support productive particle release. While previous work indicated that RANBP2 is a co-factor for the infection by some viruses^{30–35}, this study reveals an opposite role in IAV infection, namely the restriction of key nuclear transport steps.

RANBP2 can regulate the nucleocytoplasmic transport of macromolecules by two major mechanisms, first by regulating the cycle of Ran, second by interacting with nuclear transport receptors^{22,23}. The replication of IAV involves four distinct sequential NCT steps, namely the import of incoming vRNPs, the export of viral mRNAs, the import of translated viral proteins, and the export of vRNPs. RANBP2 was found to regulate only two of these steps, suggesting a specific mechanism. Specifically, RANBP2 was not involved in the initial entry



of incoming vRNPs into the nucleus, which involves the classical karyopherin α/β nuclear import pathway^{14,44,45}, and did not seem to affect the initial export of viral transcripts, which involves the general mRNA export pathway via NXF1:NXT1⁴⁶⁻⁴⁹. Rather, RANBP2 acted on late nuclear transport steps of IAV, after translation of the viral proteins. First, RANBP2 was found to regulate the re-import of the polymerase complex subunits, which is known to involve different pathways, the

best characterised being via the β -karyopherin RanBP5⁵⁰⁻⁵². Second, results suggest that RANBP2 exerts a quality control checkpoint for vRNA exported back to the cytoplasm, a step known to depend on the β -karyopherin CRM1⁵³⁻⁵⁵. Our results, therefore, suggest that RANBP2 may impact viral NCT by interacting with key β -karyopherins.

Although vRNA levels increased in RANBP2-deficient cells, infectious viral particle production did not. This likely results from the

Fig. 4 | Mislocalisation of the RANBP2-T585M ANE1 variant amplifies IAV replication and hyper-inflammation. **a** CRISPR/Cas9 editing strategy introducing the C1754T mutation (p.T585M) into RANBP2 via homology-directed repair (HDR). Resulting clones included WT homozygous clones, WT/C1754T heterozygous, and C1754T/C1754T homozygous genotypes. **b** RNA expression of WT and C1754T alleles was assessed by RANBP2-specific RTqPCR. HEK-293T cells transfected with WT, T585M or both forms served as controls (technical replicates from a single experiment; mean \pm SD). **c** RANBP2 sequence positions 1749–1757 showing C > T substitution at 1754 (c.C1754T), resulting in the p.T585M mutation. **d** Sanger sequencing confirmed genotypes of CRISPR clones, showing C, T, or both at position 1754. **e** NP staining in CRISPR clones infected with IAV (MOI 0.5) at 8 hpi; additional representative fields are shown in Figure S16. **f** Cytoplasmic NP

fluorescence quantification ($p < 0.0001$). **g** Viral RNA levels (M1 segment) at 1, 8 and 24 hpi normalized to 1 h; statistical significance by two-way ANOVA (Fig. S17). **h** Pro-inflammatory cytokine transcripts (CXCL10, IL-6, IL-1 β , CXCL8, CCL3) after overnight infection, normalized to RPL13a and WT clone C4; significance by one-way ANOVA (Fig. S18). For qPCR quantifications (**g**, **h**), data are shown as mean \pm SEM ($n = 4$). **i**, **j** RANBP2 and FG-repeat staining in CRISPR clones, with enlarged rim views. **k** Nuclear rim RANBP2 fluorescence quantification (C10, $p = 0.006$; C6-C9-C14, $p < 0.0001$). Confocal images (**e**, **i–k**) represent $n = 3$ independent experiments; scale bars: 20 μ m. Imaging quantifications (**f**, **k**) shown as violin plots ($n = 3$). Box-and-whisker plots (**g**, **h**) display median, 25th–75th percentiles, min/max. Statistical tests: one-way ANOVA (**f**, **k**). ns: non-significant.

disproportionate accumulation of some vRNA segments in the cytoplasm observed in RANBP2-KD cells, which could impair packaging. The resulting cytoplasmic vRNA can activate RIG-I, which results in the production of pro-inflammatory cytokines through NF- κ B signalling⁵⁶. Consistent with this, RANBP2-KD cells exhibited a pronounced inflammatory response following IAV infection, characterised by elevated chemokine production and secretion. Although there was considerable variability in the magnitude of this effect across experiments, as well as differences in the cytokines induced, particularly when comparing non-immune cell lines (A549, U2OS) with primary immune cells (macrophages), the global increase in inflammatory activation upon RANBP2 KD was consistently observed. Our findings therefore suggest that the abnormal cytoplasmic accumulation of vRNA segments may act as PAMPs that amplify the inflammatory response during IAV infection.

Influenza viruses are the predominant viral trigger of ANE1 and reasons for this remain unclear^{4–9}. In particular, the high prevalence for Influenza over other respiratory infections (e.g., RSV, SARS-CoV-2) and other childhood febrile illnesses (e.g., streptococcal infections) is puzzling and unexplained. Our work suggests that, by restraining key steps of IAV NCT, RANBP2 is required to limit the accumulation of viral PAMPs in the cytoplasm.

RANBP2 pathogenic variants are known to be heterozygous dominant point mutations, yet their underlying molecular mechanism remains not known. We previously reported that both wild-type and mutant RANBP2 alleles are co-expressed in ANE1 patients⁴³, suggesting a possible gain-of-function or dominant-negative effect. However, exogenous T585M RANBP2 is expressed normally and localises correctly to the nuclear envelope^{27,28}, arguing against a dominant-negative mechanism. Still, overexpression studies may not reflect the physiological balance of wild-type and mutant protein in patients, and the use of artificial tags could perturb natural functions and interactions.

Here, using CRISPR knock-in clones, we demonstrate that the T585M mutation prevents RANBP2 from properly associating with the nuclear envelope, which is consistent with the fact that most ANE1 variants cluster within the NTD responsible for NPC anchoring. Importantly, the T585M mutation phenocopied RANBP2 knockdown in their effects of viral replication and inflammatory responses, supporting a haploinsufficiency mechanism that reflects a specific loss of RANBP2 function at the nuclear envelope rather than a global reduction in RANBP2 protein. In heterozygous cells, only partial RANBP2 localisation to the nuclear envelope was observed, further supporting this model. Notably, RANBP2 has a pLI (probability of Loss-of-function Intolerance) score of 1 in gnomAD, indicating strong intolerance to loss of function variants, and confirming the essential role of its proper expression and localisation at the nuclear pore complex in ANE1 pathogenesis.

This study provides the first direct evidence that an ANE1-associated mutation enhances IAV-induced inflammatory responses. This phenotype was equally pronounced in homozygous and heterozygous ANE1 clones, indicating that even partial mislocalisation of RANBP2 can markedly amplify IAV-triggered inflammation. This role of

RANBP2 in restraining virus-induced hyperinflammation is consistent with the elevated pro-inflammatory cytokine levels reported in ANE1 patients, most of whom carry heterozygous RANBP2 mutations, with only a single case of biallelic case described⁵⁷. However, this work does not yet explain how increased peripheral inflammation leads to encephalopathy in patients. Future studies in individuals carrying ANE1 mutations will be essential to define how these variants affect the composition and function of innate immune cell populations. Moreover, since there is currently no evidence of innate immune cell infiltration in patient brains during ANE1 episodes, animal models will be critical to assess how neurons and glia contribute to disease onset.

Methods

Ethics statement

No animal experiments were conducted in this study. Human PBMCs were isolated from de-identified blood samples obtained from the Etablissement Français du Sang (EFS) Occitanie upon signed informed consent from donors.

Viruses, lentiviral vectors and cells

Infections with IAV were carried out with the H1N1/A/WSN/1933 strain in all experiments, except for the Alpha-Centauri assay, where this same strain was engineered to express a fragment of the NanoLuc (IAV- α), as described below. Lentiviral vectors (LV) were produced in HEK-293T cells (ATCC) by calcium phosphate transfection using a VSV-G envelope plasmid (pVSVg; 15 μ g in a 70–80% confluent 175 cm² flask), a Gag-Pol encapsidation plasmid (p8.74; 30 μ g), and the transfer plasmid of interest (30 μ g; mCherry-shRNA-control, mCherry-shRNA-RANBP2, or Cen-NLS; see Table S1). After 48 h, vectors were harvested and ultracentrifuged for 1 h at 82,000 \times g (Optima XE-90, Beckman Coulter) at 4 $^{\circ}$ C. A549 cells (ATCC) and CRISPR-engineered U2OS clones (generated in-house) were cultured in Dulbecco's Modified Eagle Medium (DMEM, Gibco) supplemented with 10% of Foetal bovine serum (FBS, Serana) and 1 \times penicillin/streptomycin (PS, Gibco) at 37 $^{\circ}$ C with 5% CO₂. THP-1 cells and monocyte-derived macrophages (MDM) were cultured in Roswell Park Memorial Institute (RPMI-1640, Gibco) medium supplemented with 10% FBS and 1 \times of PS. MDCK cells (ATCC) were cultured in Minimum Essential Medium (MEM, Gibco) supplemented with 5% FBS and 1 \times of PS.

Lentiviral transduction

Cells were seeded into plates one day prior to transduction. After a PBS wash, lentiviral transduction was performed at MOI 20 to 40 (transducing units/cell) in a small volume of culture medium supplemented with 2% FBS, to facilitate viral adsorption. After 2 h of incubation at 37 $^{\circ}$ C, 10% FBS culture medium was added. Transduced cells were cultured for 48–72 h prior to viral infections to allow efficient knock-down. All experiments were completed by 56–96 h post-transduction.

Viral production

H1N1/A/WSN/1933 viral stocks were produced by amplification at an MOI of 10⁻⁴ on MDCK cells, cultured in MEM containing 2%-FBS and

1 µg/mL of TPCK-treated trypsin for 3 days at 37 °C. Viral supernatants were harvested and centrifuged for 5 min at 2000 *g* to remove cellular debris. Aliquots were stored at –80 °C. IAV titres were determined by TCID50 assay as described below.

IAV infections

Cells were infected with IAV at MOI 0.5 for all experiments, except when monitoring the early steps of the viral cycle (i.e. internalization and nuclear import), where MOI 4 was used to increase signal detection. Cells were exposed to IAV for 1 h in a small volume of 2% FBS culture medium to promote viral adsorption at the cell surface before replacing the inoculum with warm culture medium and incubating at 37 °C with 5% CO₂.

RNA extractions and RTqPCR

Intracellular RNA was extracted using the RNeasy mini kit (Qiagen) according to the manufacturer's protocol. RNA yield and purity were assessed by spectrophotometry (NanoDrop 2000c, ThermoFisher Scientific). Reverse transcription (RT) using oligo(dT) and random primers was performed using the PrimeScript RT Reagent Kit (Perfect Real Time, Takara Bio Inc). Strand-specific RT for IAV RNA was performed using tagged primers that bind either to the consensus 3'-end sequence of vRNA or cRNA of all 8 segments, with Superscript III (Invitrogen, ThermoFisher Scientific) in the presence of 0.1M DTT (Invitrogen, ThermoFisher Scientific), 10 mM dNTP (Invitrogen, ThermoFisher Scientific), and RNasin (Promega). Segment distinction was then achieved by qPCR using specific primer pairs. RANBP2-specific RT was performed using a primer (1 µM) binding to a region absent from RGPDs, as described in ref. 43 and the PrimeScript RT Reagent Kit. Real-time quantitative PCR was performed using the Power Up kit (Applied Biosystems, ThermoFisher Scientific) on the ViiA7 thermocycler (Life technologies, ThermoFisher Scientific). All RT and qPCR primers are listed in Table S2.

Immunofluorescence

Cells were washed with PBS and fixed with 4% paraformaldehyde (PFA, ThermoFisher Scientific) for 10 min at room temperature (R/T). After 3 PBS washes, remaining PFA was quenched with PBS NH₄Cl 50 mM for 10 min at R/T. Cells were then permeabilized using PBS 0.5% Triton-100X (Sigma Aldrich) for 15 min at R/T, and saturated in PBS 2% Normal goat serum (NGS, Invitrogen, ThermoFisher Scientific) with 2 PBS washes between each step. Incubation with primary antibodies for 1 h at R/T was followed by 5 PBS washes and incubation with secondary antibodies for 30 min at R/T (Table S3). After further washing, cells were stained with Hoechst (1:10,000 dilution in PBS; ThermoFisher Scientific) for 5 min at R/T, washed, and mounted in Prolong Diamond Antifade mounting medium (Invitrogen, ThermoFisher Scientific). Images were acquired on a Zeiss LSM880 Airyscan confocal microscope at the Montpellier Ressources Imagerie (MRI) facility and processed using Fiji (2.14.0). For visualisation, Alexafluor-488 signal corresponding to NP was pseudocoloured ("Orange Hot") and brightness was increased uniformly across conditions.

Alpha-Centauri assay

Cloning of IAV-α. A DNA fragment coding for αNluc (GVTGWRLCER-ILA) flanked by NotI and NheI overhangs was obtained by annealing two overlapping oligonucleotides:

NotI-αNluc-NheI-F GGCCGCAGGGGAGTGACAGGGTGGAGACTATGCGAAAGAATACTTGCATAAG

NotI-αNluc-NheI-R CTAGCTTATGCAAGTATTCTTTCGATAGTCTCCACCCTGTCACTCCCCTGC

The reverse genetics plasmid pPoll-SL-PB2-αNluc was generated by subcloning this fragment between the NotI and NheI sites of the pPoll-SL-PB2-Nanoluc⁵⁸.

Particle production by reverse genetics. The eight pPoll-WSN plasmids (-PB2-αNluc, -PBI, -PA, -HA, -NP, -NA, -NS, -M), and four expression plasmids (pcDNA3.1-WSN-PB2, -PBI, -PA, -NP; 0.5 µg of each) were co-transfected into a co-culture of 293T and MDCK cells (seeded in a 6-well plate at 4 × 10⁵ and 3 × 10⁵ cells, respectively) using 10 µL of FuGENE® HD transfection reagent (Promega). After 24 h at 35 °C, cells were washed twice with DMEM and incubated in DMEM containing 1 µg/mL of TPCK-treated trypsin for 48 h. Recombinant PB2-αNluc virus was amplified at an MOI of 10⁻⁴ on MDCK cells for 3 days at 35 °C. Viral stocks were titrated on MDCK by plaque assays and sequenced to confirm the presence of the αNluc coding sequence.

Cells were transduced with LV Cen-NLS for 3 days, followed by LV shRNA-control or LV shRNA-RANBP2 at MOI 15 for 4 days. Cells were then infected with IAV-α at MOI 4 for the indicated times. Luminescence was measured using NanoGlo Live Cell substrate (Promega) and an Infinite M Plex spectrophotometer (Tecan).

Nucleo-cytoplasmic fractionation

Nuclear and cytoplasmic fractions were separated using the NE-PER Kit (ThermoFisher Scientific) according to the manufacturer's protocol. Briefly, 1–2 × 10⁶ cells were washed in PBS, lysed in cold CER I buffer, vortexed 15 s, and incubated on ice for 10 min. Cold CER II buffer was then added, followed by brief vortexing and incubation on ice for 1 min. After 5 s vortexing and full speed centrifugation, supernatants (cytoplasmic fraction) were collected and stored at –80 °C. Nuclear pellets were resuspended in cold NER buffer and subjected to 4 cycles of 15 s vortexing then 10 min incubation on ice. After full speed centrifugation, supernatants (nuclear fraction) were collected and stored at –80 °C.

Western blot

Cell lysates were sonicated for 20 cycles (30 s on/off; Bioruptor Pico, Diagenode) and mixed with 4X Laemmli buffer (250 mM Tris-HCl pH 7, 8% sodium dodecyl sulphate (SDS), 40% glycerol, 10% β-mercaptoethanol, and 0.005% bromophenol blue). After denaturation at 95 °C for 5 min, samples underwent SDS polyacrylamide gel electrophoresis (SureCast Gel Handcast System, Thermo Fisher Scientific) and were transferred to a 0.45 µm nitrocellulose membrane (Sigma Aldrich). Membranes were saturated in PBS containing 0.05% Tween 20 (Sigma) and 10% milk powder for 30 min, incubated with primary antibodies overnight at 4 °C, washed 3 times in PBS 0.05% Tween 20, and incubated with HRP-conjugated secondary antibodies for 1 h at R/T (Table S3). Signals were detected with Immobilon Forte Western HRP substrate (Merck) or Immobilon ECL Ultra Western HRP Substrate (Merck) on a Chemidoc imaging system (Bio-Rad).

TCID50 assay

MDCK cells were seeded in FBS-free MEM medium (Gibco) and inoculated with serial dilutions of viral supernatants in 2% FBS medium in octuplicates. After 3 days at 37 °C and 5% CO₂, cells were washed twice in PBS and fixed with 4% PFA for 10 min at R/T and stained with crystal violet. TCID50 titre were calculated as:

$$\log_{10} \left(\frac{\text{TCID50}}{\text{mL}} \right) = x_0 - \left(\frac{d}{2} \right) + \left(d * \frac{xi}{n} \right) + v$$

where x_0 is the log of the initial dilution factor, d the log of the serial dilution factor, xi the number of positive events, n the number of replicates, and v the log of the inoculum volume (mL).

Peripheral blood mononuclear cell (PBMC) isolation and monocyte-derived macrophages differentiation

Buffy coats from healthy donors were obtained from the Établissement Français du Sang (EFS). Blood samples were diluted 1:1 with PBS and layered over an equivalent volume of Lymphoprep (Stemcell

technologies) at R/T. Samples were centrifuged at 800 g for 30 min at 20 °C (no brake). The PBMC ring was collected using a 5 mL pipet, washed 3 times in a final volume of 50 mL PBS (1200 rpm, 5 min, 20 °C with brakes on), and resuspended in 30 mL of 10% FBS RPMI-1640 medium. PBMCs were counted manually using counting chambers (Kova).

For MDM differentiation, 2×10^7 cells were seeded per well into 6-well plates, allowed to adhere for 45 min, at 37 °C with 5% CO₂, washed 3 times with 10% FBS RPMI-1640 medium directly on the cell layers to remove loosely attached cells, and cultured in RPMI-1640 medium with 10% FBS and 50 ng/mL GM-CSF (Gentaur) for 8 days.

Flow cytometry

After 8 days of MDM differentiation, cells were stained and analysed on a Fortessa flow cytometer (BD Biosciences) using the following antibodies: CD3-BV421 (clone UCHT1, Biolegend 300433), CD14-PerCP-Cy5.5 (clone HCD14, Biolegend 325621), CD16-Alexa700 (clone 3G8, Biolegend 302026), CD11b-APC-Cy7 (clone MI/70, Biolegend 101225), HLA-DR-FITC (REA805, Miltenyi 130-111-941), and CD80-BV650 (clone 2D10, Biolegend 305227) (see Table S3).

Multiplex Luminex assay

The presence of inflammatory mediators was assessed in supernatants of stimulated MDMs using the ProcartaPlex Human inflammation Panel 20-plex kit (Invitrogen, ThermoFisher Scientific). First, a subset of samples was centrifuged and diluted 1:10 or 1:50 to determine the optimal dilution for the assay. A 1:50 dilution was selected in order to detect the strongly induced mediators (e.g. CXCL8) within the range of the standard curves supplied in the kit. Buffers and standards were prepared according to the manufacturer's protocol. Briefly, the Capture Bead mix was vortexed and added to the plate, followed by washing with Wash buffer, then samples and standards were added. The plate was incubated for 1 h at R/T on a shaker. After 2 washes, Biotinylated Detection Antibody mix was added for 30 min at R/T on a shaker. After 2 washes, Streptavidin-PE was added for 30 min at R/T on a shaker. After 2 more washes, the plate was read on the MAGPIX flow cytometer (Luminex).

Establishment of U2OS clones expressing RANBP2 T585M by CRISPR knock-in

The plasmid pUclDT Amp (synthesized by Integrated DNA Technologies) containing the donor sequence (see below) and the plasmid pSpCas9(BB)-2A-Puro (PX459; Addgene #62988) modified to contain the guide sequence (5'-GGCAGAATGCCTTCAGAAAA-3') were co-transfected in equal amounts into human osteosarcoma U2OS cells using Lipofectamine 3000 (Invitrogen, ThermoFisher Scientific), following the manufacturer's instructions. Two days post-transfection, cells were selected with puromycin (Gibco) at 2 µg/ml for four days. Single-cell clones were obtained by limiting dilution. A total of 198 cells were distributed in 576 wells containing 10% FBS DMEM medium. After 3 weeks, 47 clones were successfully established and analyzed by RANBP2 allele-specific RTqPCR as described above and Sanger sequencing (Eurofins).

Donor DNA sequence:

(GCGGTTTGTACTCTGATTACAGAAAAGCAGTgtaagtagtaaaacaa
aaatattgcttcacttagtgctgaggtttaccggggatttaactctcatgtgagatttaattgt
catgtgaccattaacatatatgtatgtaagccctgaactgtgtatttagaaagcaatttttagtaa
ttgaactatttttagACCTGGAACGTAGCAAAATTGAGACTTCTAGTTCAG
CATGAAATAAACACTCTAAGAGCCCAGGAAAAACATGGCCTTCAACC
TGCTCTGCTTGATCATTGGGAGAGTGTCTGAGAAAAATGgtgagtttaaa
gtataagcatttttaagaacattacttaatttttaaatcatgaacttttttagaaagttttttg
ttctgaaacagcagcttggtcacattatgacagatgtgtttttattgctgcaaaatgtaattgt
agtttaaatagcacttaggaggaatgctggcacacagtgtaattgttatttagctgagc
gttactgttattcctaataaattgctgataattatcagcctgaaaataaaaaa)

Capital letters: exon

Lowercase: intron

Underlined: mutations

Bold lowercase: c. 1754 C > T mutation

Generation of homozygous/heterozygous RANBP2-expressing control cells for allelic qPCR

HEK-293T cells were transfected with plasmids encoding mCherry-RANBP2-shRNA and either GFP-RANBP2-WT, GFP-RANBP2-T585M, or both (Table S1) in calcium phosphate. After 48 h of culture, cells were detached using trypsin (Gibco) and sorted on the ARIA IIu cytometer (Becton Dickinson) at the MRI facility to isolate the mCherry-positive cells. Sorted cells were lysed and total RNAs were extracted using the RNeasy mini kit (Qiagen) according to the manufacturer's protocol.

MTT cell viability assay

Cell viability was assessed using the MTT [3-(4,5-dimethylthiazol-2-yl)-2,5-diphenyltetrazolium bromide] assay (Sigma). Following treatment, the culture medium was carefully removed, and cells were washed once with PBS to eliminate any residual medium or serum components. A stock solution of MTT was prepared at 5 mg/mL in DMEM without phenol red (Gibco). Subsequently, 100 µl of the MTT solution was added to each well and incubated for 3 h at 37 °C with 5% CO₂ to allow the formation of formazan crystals by metabolically active cells. After incubation, 100 µl of acidified isopropanol (1:200 HCl 0.05 N) was added to each well to dissolve the formazan crystals completely. The absorbance was measured at 570 nm using an Infinite M Plex spectrophotometer (Tecan).

Statistical analysis

Statistical analysis was performed using the GraphPad Prism software (v10.2.3). For qPCR experiments, statistical analyses were performed on Δ Ct or $\Delta\Delta$ Ct values, as indicated. Δ Ct values correspond to the mean of technical replicates normalised for the housekeeping gene, and $\Delta\Delta$ Ct values are normalised to the control condition. Unless otherwise stated, biological replicates are represented as single dots in bar graphs (mean +/- SEM). All statistical tests are specified in the figure legends.

Reporting summary

Further information on research design is available in the Nature Portfolio Reporting Summary linked to this article.

Data availability

Source Data are provided with this paper, including uncropped and unprocessed scans of all blots. Source data are provided with this paper.

References

- Lee, V. W. M. et al. Factors associated with outcomes of severe acute necrotizing encephalopathy: A multicentre experience in Malaysia. *Dev. Med. Child Neurol.* **65**, 1256–1263 (2023).
- Sakuma, H. et al. International consensus definitions for infection-triggered encephalopathy syndromes. *Dev. Med. Child Neurol.* **67**, 195–207 (2025).
- Wu, X. et al. Acute necrotizing encephalopathy: an under-recognized clinicoradiologic disorder. *Mediat. Inflamm.* **2015**, 792578 (2015).
- Mizuguchi, M., Yamanouchi, H., Ichiyama, T. & Shiomi, M. Acute encephalopathy associated with influenza and other viral infections. *Acta Neurol. Scand.* **115**, 45–56 (2007).
- Bartolini, L. et al. Severe A(H1N1)pdm09 influenza acute encephalopathy outbreak in children in Tuscany, Italy, December 2023 to January 2024. *Eurosurveillance* **29**, 2400199 (2024).

6. Jiang, J., Wang, Y. E., Palazzo, A. F. & Shen, Q. Roles of Nucleoporin RanBP2/Nup358 in Acute Necrotizing Encephalopathy Type 1 (ANE1) and viral infection. *Int. J. Mol. Sci.* **23**, 3548 (2022).
7. Neilson, D. E. et al. Autosomal dominant acute necrotizing encephalopathy. *Neurology* **61**, 226–230 (2003).
8. Chatur, N., Yea, C., Ertl-Wagner, B. & Yeh, E. A. Outcomes in influenza and RANBP2 mutation-associated acute necrotizing encephalopathy of childhood. *Dev. Med. Child Neurol.* **64**, 1008–1016 (2022).
9. Bashiri, F. A. et al. Acute necrotizing encephalopathy of childhood: a multicenter experience in Saudi Arabia. *Front. Pediatr.* **8**, 564934 (2020).
10. Levine, J. M., Ahsan, N., Ho, E. & Santoro, J. D. Genetic acute necrotizing encephalopathy associated with RANBP2: clinical and therapeutic implications in pediatrics. *Mult. Scler. Relat. Disord.* **43**, 102194 (2020).
11. Sugaya, N. Influenza-associated encephalopathy in Japan. *Semin. Pediatr. Infect. Dis.* **13**, 79–84 (2002).
12. Koh, J. C., Murugasu, A., Krishnappa, J. & Thomas, T. Favorable outcomes with early Interleukin 6 receptor blockade in severe acute necrotizing encephalopathy of childhood. *Pediatr. Neurol.* **98**, 80–84 (2019).
13. Okumura, A. et al. Outcome of acute necrotizing encephalopathy in relation to treatment with corticosteroids and gammaglobulin. *Brain Dev.* **31**, 221–227 (2009).
14. Dou, D., Revol, R., Östbye, H., Wang, H. & Daniels, R. Influenza A virus cell entry, replication, virion assembly and movement. *Front. Immunol.* **9**, 383042 (2018).
15. Carter, T. & Iqbal, M. The Influenza A virus replication cycle: a comprehensive review. *Viruses* **16**, 316 (2024).
16. Fodor, E. & Velthuis, A. J. W. T. Structure and function of the Influenza virus transcription and replication machinery. *Cold Spring Harb. Perspect. Med.* **10**, 1–14 (2020).
17. Zhu, Z., Fodor, E. & Keown, J. R. A structural understanding of influenza virus genome replication. *Trends Microbiol.* **31**, 308–319 (2023).
18. Mettelman, R. C. & Thomas, P. G. Human susceptibility to influenza infection and severe disease. *Cold Spring Harb. Perspect. Med.* **11**, a038711 (2021).
19. Clohisey, S. & Baillie, J. K. Host susceptibility to severe influenza A virus infection. *Crit. Care* **23**, 303 (2019).
20. Gounder, A. P. & Boon, A. C. M. Influenza pathogenesis: the effect of host factors on severity of disease. *J. Immunol.* **202**, 341–350 (2019).
21. Neilson, D. E. et al. Infection-triggered familial or recurrent cases of acute necrotizing encephalopathy caused by mutations in a component of the nuclear pore, RANBP2. *Am. J. Hum. Genet.* **84**, 44–51 (2009).
22. Yokoyama, N. et al. A giant nucleopore protein that binds Ran/TC4. *Nature* **376**, 184–188 (1995).
23. Hutten, S., Flotho, A., Melchior, F. & Kehlenbach, R. H. The Nup358-RanGAP complex is required for efficient Importin α / β -dependent nuclear import. *Mol. Biol. Cell* **19**, 2300 (2008).
24. Desgraupes, S., Etienne, L. & Arhel, N. J. RANBP2 evolution and human disease. *FEBS Lett.* **597**, 2519–2533 (2023).
25. Desgraupes, S. & Arhel, N. Unraveling the diversity of RANBP2: protein isoforms and implications for cellular function and human disease. *J. Mol. Biol.* **437**, 169452 (2025).
26. Joseph, J. & Dasso, M. The nucleoporin Nup358 associates with and regulates interphase microtubules. *FEBS Lett.* **582**, 190–196 (2008).
27. Shen, Q. et al. RanBP2/Nup358 enhances miRNA activity by sumoylating Argonautes. *PLoS Genet.* **17**, e1009378 (2021).
28. Bley, C. J. et al. Architecture of the cytoplasmic face of the nuclear pore. *Science* **376**, eabm9129 (2022).
29. Carlon-Andres, I. et al. Nup358 and Transportin 1 cooperate in adenoviral genome import. *J. Virol.* **94**, e00164–20 (2020).
30. Copeland, A. M., Newcomb, W. W. & Brown, J. C. Herpes simplex virus replication: roles of viral proteins and nucleoporins in capsid-nucleus attachment. *J. Virol.* **83**, 1660–1668 (2009).
31. Hofemeister, H. & O'Hare, P. Nuclear pore composition and gating in Herpes Simplex virus-infected cells. *J. Virol.* **82**, 8392–8399 (2008).
32. Bichel, K. et al. HIV-1 capsid undergoes coupled binding and isomerization by the nuclear pore protein NUP358. *Retrovirology* **10**, 81 (2013).
33. Di Nunzio, F. et al. Human Nucleoporins promote HIV-1 docking at the nuclear pore, nuclear import and integration. *PLoS One* **7**, e46037 (2012).
34. Schaller, T. et al. HIV-1 Capsid-Cyclophilin interactions determine nuclear import pathway, integration targeting and replication efficiency. *PLoS Pathog.* **7**, e1002439 (2011).
35. Zhang, R., Mehla, R. & Chauhan, A. Perturbation of host nuclear membrane component RanBP2 impairs the nuclear import of human immunodeficiency Virus –1 Preintegration Complex (DNA). *PLoS One* **5**, e15620 (2010).
36. Khanna, M. et al. Unravelling the interaction between Influenza virus and the nuclear pore complex: insights into viral replication and host immune response. *VirusDisease* **35**, 231–242 (2024).
37. Watanabe, T., Watanabe, S. & Kawaoka, Y. Cellular networks involved in the influenza virus life cycle. *Cell Host Microbe* **7**, 427–439 (2010).
38. Munier, S., Rolland, T., Diot, C., Jacob, Y. & Naffakh, N. Exploration of binary virus-host interactions using an infectious protein complementation assay. *Mol. Cell. Proteom.* **12**, 2845–2855 (2013).
39. Maarifi, G. et al. RanBP2 regulates the anti-retroviral activity of TRIM5 α by SUMOylation at a predicted phosphorylated SUMOylation motif. *Commun. Biol.* **1**, 1–11 (2018).
40. Portilho, D. M. et al. Endogenous TRIM5 α function is regulated by SUMOylation and nuclear sequestration for efficient innate sensing in dendritic cells. *Cell Rep.* **14**, 355–369 (2016).
41. Li, J. et al. RanBP2/Nup358 mediates sumoylation of STAT1 and antagonizes Interferon- α -mediated antiviral innate immunity. *Int. J. Mol. Sci.* **25**, 299 (2024).
42. Fernandez, J. et al. Measuring the subcellular compartmentalization of viral infections by protein complementation assay. *Proc. Natl. Acad. Sci. USA.* **118**, e2010524118 (2021).
43. Gouy, B. et al. Rapid and inexpensive bedside diagnosis of RAN binding protein 2-associated acute necrotizing encephalopathy. *Front. Neurol.* **14**, 1282059 (2023).
44. Miyake, Y. et al. Influenza virus uses transportin 1 for vRNP debundling during cell entry. *Nat. Microbiol.* **4**, 578–586 (2019).
45. Nguyen, N. L. T., Wu, W. & Panté, N. Contribution of the nuclear localization sequences of Influenza A nucleoprotein to the nuclear import of the influenza genome in infected cells. *Viruses* **15**, 1641 (2023).
46. Bhat, P. et al. Influenza virus mRNAs encode determinants for nuclear export via the cellular TREX-2 complex. *Nat. Commun.* **14**, 1–14 (2023).
47. Zhao, L. et al. TREX (transcription/export)-NP complex exerts a dual effect on regulating polymerase activity and replication of influenza A virus. *PLoS Pathog.* **18**, e1010835 (2022).
48. Zhang, K. et al. Cellular NS1-BP protein interacts with the mRNA export receptor NXF1 to mediate nuclear export of influenza virus M mRNAs. *J. Biol. Chem.* **300**, 107871 (2024).
49. Pereira, C. F., Read, E. K. C., Wise, H. M., Amorim, M. J. & Digard, P. Influenza A Virus NS1 protein promotes efficient nuclear export of unspliced viral M1 mRNA. *J. Virol.* **91**, (2017).

50. Huet, S. et al. Nuclear import and assembly of influenza A virus RNA polymerase studied in live cells by fluorescence cross-correlation spectroscopy. *J. Virol.* **84**, 1254–1264 (2010).
 51. Hemerka, J. N. et al. Detection and characterization of influenza A virus PA-PB2 interaction through a bimolecular fluorescence complementation assay. *J. Virol.* **83**, 3944–3955 (2009).
 52. Cros, J. F., Garcia-Sastre, A. & Palese, P. An Unconventional NLS is critical for the nuclear import of the Influenza A Virus Nucleoprotein and Ribonucleoprotein. *Traffic* **6**, 205–213 (2005).
 53. Elton, D. et al. Interaction of the influenza virus nucleoprotein with the cellular CRM1-mediated nuclear export pathway. *J. Virol.* **75**, 408–419 (2001).
 54. Ma, K., Roy, A. M. M. & Whittaker, G. R. Nuclear export of influenza virus ribonucleoproteins: identification of an export intermediate at the nuclear periphery. *Virology* **282**, 215–220 (2001).
 55. Watanabe, K. et al. Inhibition of nuclear export of ribonucleoprotein complexes of influenza virus by leptomycin B. *Virus Res* **77**, 31–42 (2001).
 56. Iwasaki, A. & Pillai, P. S. Innate immunity to influenza virus infection. *Nat. Rev. Immunol.* **14**, 315–328 (2014). 2014 14:5.
 57. Ayaz, A., Doğru, Z., Kılıç, B. & Süzek, B. E. First case with RANBP2 biallelic mutation and severe acute necrotizing encephalopathy phenotype. *Clin. Neurol. Neurosurg.* **221**, 107418 (2022).
 58. Diot, C. et al. Influenza A virus polymerase recruits the RNA Helicase DDX19 to promote the nuclear export of viral mRNAs. *Sci. Rep.* **6**, 1–12 (2016).
- analysed the data. S.D. and N.J.A wrote the manuscript. S.M. and A.F.P provided essential reagents and helped interpret the results. N.J.A coordinated the project. All authors contributed to revising the manuscript.

Competing interests

The authors declare no competing interests.

Additional information

Supplementary information The online version contains supplementary material available at <https://doi.org/10.1038/s41467-026-69288-1>.

Correspondence and requests for materials should be addressed to Nathalie J. Arhel.

Peer review information *Nature Communications* thanks Robert Chua, and the other, anonymous, reviewer(s) for their contribution to the peer review of this work. A peer review file is available.

Reprints and permissions information is available at <http://www.nature.com/reprints>

Publisher's note Springer Nature remains neutral with regard to jurisdictional claims in published maps and institutional affiliations.

Open Access This article is licensed under a Creative Commons Attribution 4.0 International License, which permits use, sharing, adaptation, distribution and reproduction in any medium or format, as long as you give appropriate credit to the original author(s) and the source, provide a link to the Creative Commons licence, and indicate if changes were made. The images or other third party material in this article are included in the article's Creative Commons licence, unless indicated otherwise in a credit line to the material. If material is not included in the article's Creative Commons licence and your intended use is not permitted by statutory regulation or exceeds the permitted use, you will need to obtain permission directly from the copyright holder. To view a copy of this licence, visit <http://creativecommons.org/licenses/by/4.0/>.

© The Author(s) 2026

Acknowledgements

This work was financed by grants from the Agence Nationale de la Recherche (ANR-23-CE15-0005-01) and ANRS-MIE (ECTZ209411) to N.J.A., and a Canadian Institutes of Health Research (FRN 102725) grant to A.F.P. We thank Marion Cannac (Université de Montpellier, France) for help with phenotyping primary macrophages, and Montpellier Ressources Imagerie (MRI) for support with flow cytometry, cell sorting, and imaging. We thank Jomon Joseph (National Center for Cell Science, Pune, India) for the GFP-RANBP2 construct, and Sébastien Nisole (INSERM, Montpellier, France; INRS, Institut Armand Frappier, Montréal, Canada) for the GFP-RANBP2-T585M construct.

Author contributions

S.D. and N.J.A conceptualised and designed the study. S.D., A.D., S.P., B.G. performed the experiments with additional support from Y.E.W. S.D